ACS APPLIED MATERIALS & INTERFACES

www.acsami.org

Research Article

Molybdenum Oxide/Tungsten Oxide Nano-heterojunction with Improved Surface-Enhanced Raman Scattering Performance

Songyang Xie,[⊥] Dong Chen,[⊥] Chenjie Gu,* Tao Jiang,* Shuwen Zeng,* Ying Ying Wang, Zhenhua Ni, Xiang Shen, and Jun Zhou

Cite This: *ACS Appl. Mater. Interfaces* 2021, 13, 33345−33353

Read Online

ACCESS | Metrics & More | Article Recommendations | Supporting Information

ABSTRACT: By virtue of their high uniformity and stability, metal oxide-based surface-enhanced Raman spectroscopy (SERS) substrates have attracted enormous attention for molecular trace detection. However, strategies for further enhancing the SERS sensitivity are still desired. Herein, MoO_x/WO_x nano-heterojunctions are constructed by mixing MoO_x and WO_x together (MoO_x/WO_x hybrid) with diverse weight ratios. Using a 532 nm laser as the excitation source and R6G as the Raman reporter, it is shown that the Raman signal intensity (for the peak @ 1360 cm^{-1}) obtained on the optimal MoO_x/WO_x hybrid (MoO_x/WO_x = 1:1/3) is twice that observed on a pure MoO_x or WO_x substrate. Moreover, a limit of detection of 10^{-8} M and an enhancement factor of 10^8 are achieved. In the SERS enhancement mechanism investigation, it is revealed that MoO_x and WO_x form a staggered band structure. During the SERS measurement, electron−hole pairs are generated in the nano-heterojunction using the incident laser. They are then separated by the built-in potential with the electrons moving toward WO_x. The accumulated electrons on WO_x are further transferred to the R6G molecules through the coupling of orbitals. Consequently, the molecular polarizability is amplified, and SERS performance is enhanced. The abovementioned explanation is supported by the evidence that the contribution of the chemical enhancement mechanism in the optimal MoO_x/WO_x hybrid substrate is about 2.5 times or 5.9 times that in the pure WO_x or MoO_x substrate.

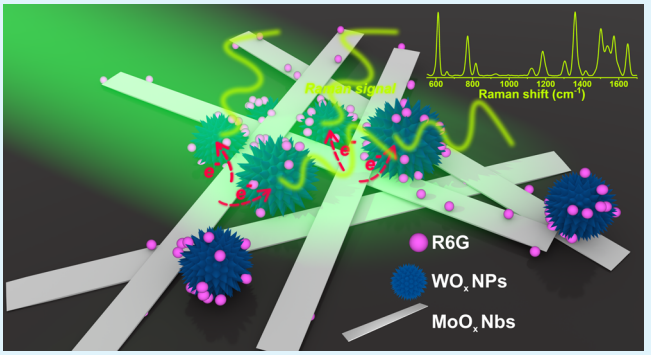

KEYWORDS: *SERS, molybdenum oxides, tungsten oxides, nano-heterojunction, charge transfer*

1. INTRODUCTION

Surface-enhanced Raman spectroscopy (SERS) was first discovered on a roughed silver electrode by Fleischmann in 1974.[1] From then on, it has been intensively studied for the understanding of the underlying mechanisms and the potential applications.[2−5] Many studies have manifested that the electromagnetic enhancement (EM) and chemical enhancement (CM) are two principal mechanisms for the SERS enhancement.[6] Owing to its virtues of ultrahigh sensitivity and specificity, the SERS technique has been widely used in the fields of chemical engineering, environment protection, food safety, bio-sensing, and so forth.[7−11]

In the early days, noble metal (e.g., Au and Ag)-based SERS substrates were extensively studied. Relying on the significantly enhanced surface electromagnetic field ($|E|$) or "hot spots" produced by the surface plasmon resonance (SPR) on the noble metal nanostructures, the Raman vibrational intensity can be magnified using $|E|^4$.[12] Over the past decades, tremendous efforts have been put on designing and preparing noble metal nanostructures with various morphologies and compositions, and great success on SERS performance improvement has been achieved.[13−19] However, from these research studies, it is clear that facile and green preparation of noble metal nanostructures/nanoparticles remains as a major challenge. In addition, the demand of substrate stability, biocompatibility, and large-scale uniformity for novel sensing applications would further limit the practicality of noble metal-based SERS substrates.[20]

More recently, the rise of novel material synthesis and defect engineering technology has triggered intensive studies of the SERS effect in functional oxide materials. For example, Yang et al. reported impressive SERS performance measured on TiO_2 nanoparticles prepared by the sol-hydrothermal method.[21] Their study showed that the Raman vibration of 4-MBA molecules at 1594 and 1078 cm^{-1} was significantly enhanced by the TiO_2 nanoparticles assembled on a silicon substrate. However, the enhancement was eliminated after calcining the

Received: February 28, 2021
Accepted: June 28, 2021
Published: July 7, 2021

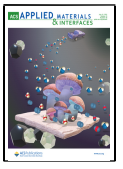

https://doi.org/10.1021/acsami.1c03848
ACS Appl. Mater. Interfaces 2021, 13, 33345−33353

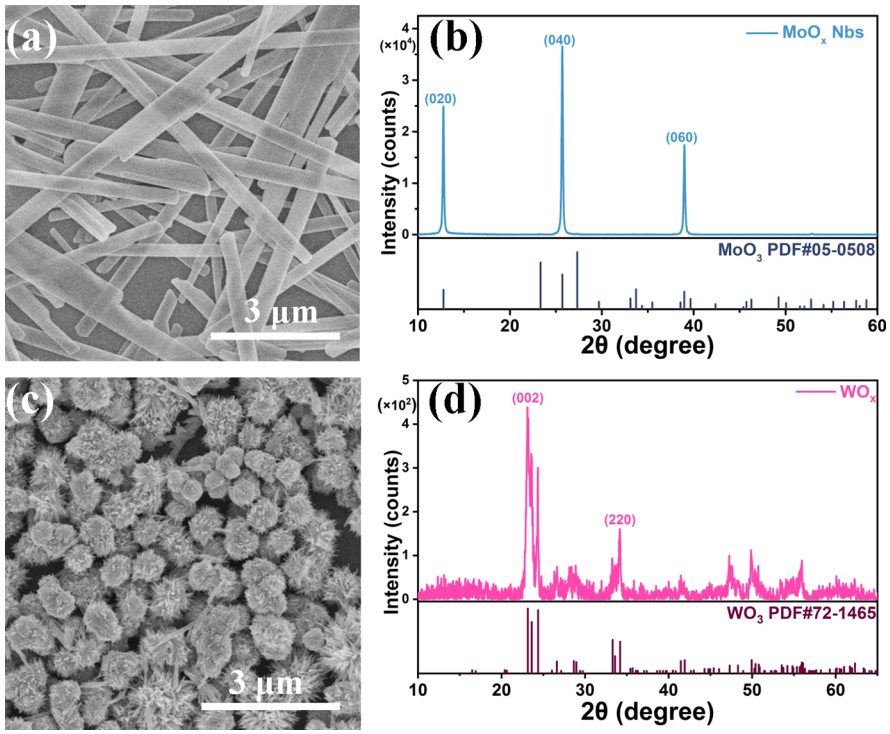

Figure 1. (a) SEM image of the synthesized MoO_x Nbs. (b) Corresponding XRD pattern of the synthesized MoO_x Nbs. (c) SEM image of the synthesized WO_x. (d) Corresponding XRD pattern of the synthesized WO_x.

TiO_2 nanoparticles in air. Based on the experimental evidence, they inferred that the SERS enhancement arose from defect level-assisted charge transfer between the defective TiO_2 nanoparticles and molecules. The transfer amplified the molecular polarizability derivative and consequently boosted the SERS performance via the CM mechanism.[22] Additionally, material engineering methods such as electrical stressing, chemical reduction, and oxygen insertion have been used to introduce defects in transitional metal oxides (MoO_{3-x}, WO_x, Cu_2O, and ZnO) and two-dimensional materials (MoS_2, HfS_2, black phosphorous, MXenes, graphene oxide, etc.). Benefiting from the enhanced charge transfer provided by the defect levels, highly stable, uniform, and bio-compatible SERS substrates with attractive performance also have been achieved.[23−34] On the other hand, theoretical and experimental studies have revealed that the free electron concentration of the oxide can be extensively tuned via defect engineering. Consequently, strong SPR can also be excited on the defective oxide using the visible light.[35] In the literature, widely tunable localized SPR was reported on MoO_{3-x} and WO_x through controlling their stoichiometry, and using Rhodamine 6G (R6G) molecules as the Raman reporter, a noble metal-comparable SERS enhancement factor of 10^8 was achieved.[36]

At this stage, it is known that the enhancement obtained on oxide-based SERS substrates not only involves the CM mechanism but may also include the EM mechanism depending on the material property.[37−39] Therefore, in order to further promote the SERS performance of these substrates, improving the SPR strength and charge transfer efficiency is a crucial aim for oxide property tuning.[40] Recently, Li et al. prepared a hybrid substrate involving molybdenum and tungsten oxides (MWO) for SERS enhancement study. By taking advantage of the inter-doping mechanism between molybdenum and tungsten oxides, extra free electrons and defect levels were generated by the interstitial defects and oxygen vacancies, which enhanced both the SPR strength and charge transfer efficiency. SERS measurement on the MWO substrate revealed an appealing SERS performance with an enhancement factor of 10^7.[41] On the other hand, researchers also developed heterojunctions for charge transfer improvement.[42−44] For example, Ghopry et al. constructed MoS_2 nanodome/graphene van der Waals heterojunctions as non-noble metal-based SERS substrates.[45] Their work showed that the heterojunctions raise the electric dipole moment and dipole−dipole interaction, which in turn facilitated the charge transfer and enhanced the overall SERS signal. Similarly, SERS improvement was also observed on the $W_{18}O_{49}$/monolayer MoS_2 heterojunctions, which was ascribed to the generation of extra excitation resonance on MoS_2.[46] At this moment, it should be pointed out that details of the charge transfer process and optimization of the charge transfer efficiency in the heterojunction are still ambiguous. Additionally, the SERS improvement produced by the heterojunction usually comprises two mechanisms, and a clear distinction on the contributions of the EM and CM mechanism to the total SERS enhancement is still unavailable.

Herein, we report the preparation of MoO_x/WO_x hybrid SERS substrates by mixing MoO_x and WO_x with diverse weight ratios (MoO_x/WoO_x = 1:0, 1:1/3, 1:1, 1:3, and 0:1). The SERS performance is evaluated using a 532 nm laser as the excitation source and R6G molecule as the Raman reporter. Through varying the weight ratios, MoO_x/WO_x hybrids with different SERS activities are obtained. More specifically, we show that the Raman signal (R6G Raman peak@1360 cm^{-1}) produced by the optimal MoO_x/WO_x hybrid (MoO_x/WoO_x = 1:1/3) is about twice as high as that observed on the pure MoO_x or WO_x substrate. The limit of detection can be as low as 10^{-8} M with an enhancement factor

https://doi.org/10.1021/acsami.1c03848
ACS Appl. Mater. Interfaces 2021, 13, 33345−33353

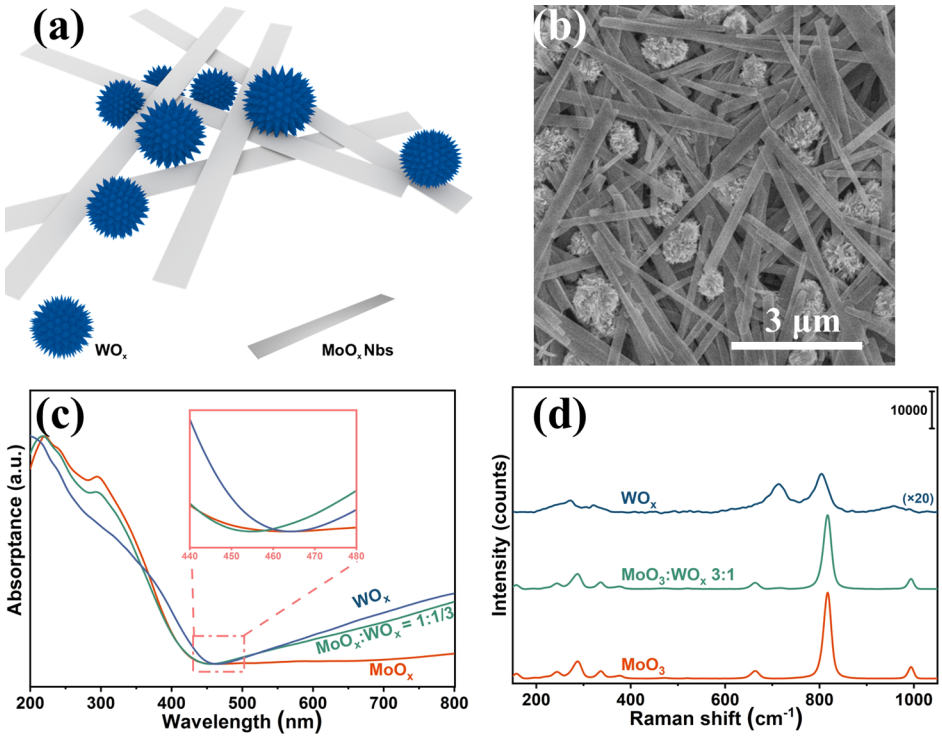

Figure 2. (a) Schematic illustration of the nano-heterojunction in the MoO_x/WO_x hybrids. (b) SEM image of the MoO_x/WO_x hybrids with the weight ratio = 1:1/3. (c) UV−vis absorption spectra of MoO_x, WO_x, and MoO_x/WO_x hybrids (MoO_x/WO_x = 1:1/3). (d) Raman spectra of MoO_x, WO_x, and MoO_x/WO_x hybrids (MoO_x/WO_x = 1:1/3).

of 10^8. Furthermore, mechanism investigation is performed. Our study shows that MoO_x and WO_x form a staggered band structure. During SERS measurement, the incident laser generates many electron−hole pairs in the nano-heterojunctions. The electron−hole pairs are separated by the built-in potential, and the electrons move toward the WO_x. Electrons that accumulate on the WO_x are further transferred to the R6G molecules through the coupling of the oxide and molecule orbitals. This transfer of charge in turn promotes the SERS performance. The abovementioned explanation is supported by the evidence that the contribution of the CM mechanism to the total SERS enhancement on the optimal MoO_x/WO_x hybrid is about 2.5 times and 5.9 times that observed on the WO_x and MoO_x substrate, respectively.

2. RESULTS AND DISCUSSION

MoO_x was prepared by a simple hydrothermal method, while WO_x was prepared by a solvothermal method.[23,36] Then, MoO_x and WO_x were mixed with different weight ratios (MoO_x/WoO_x = 1:0, 1:1/3, 1:1, 1:3, and 0:1) to construct the nano-heterojunctions (details in the Materials and Experimental Methods). The morphologies and crystal phases of the synthesized MoO_x and WO_x were detected by scanning electron microscopy (SEM) and X-ray diffraction (XRD), respectively. It can be seen in Figure 1a that the MoO_x shows a belt-like structure with a width of 100−1000 nm and a length of up to 10 μm. Meanwhile, the XRD pattern in Figure 1b reveals sharp diffraction peaks at (020), (040), and (060) crystal faces, which confirm a monoclinic phase. On the other hand, the SEM image of WO_x in Figure 1c shows a sea urchin-like shape with an average size of 1.0 μm. The XRD pattern in Figure 1d shows a clear reflectance peak at (002) and (220) crystal faces, indicating that WO_x also has a monoclinic phase.

The MoO_x/WO_x hybrids (Figure 2a) were also examined using SEM. Figure 2b shows that the sea urchin-like WO_x is adsorbed on the belt-like MoO_x. Comparing the SEM images of hybrids with different MoO_x/WO_x weight ratios (Figure S1, Supporting Information), it is found that the number of adsorbed WO_x on a single MoO_x belt varies with the weight ratio, which indicates that the overall number of nano-heterojunctions in each hybrid is different. Additionally, the absorption spectra of MoO_x, WO_x, and the MoO_x/WO_x hybrid with a MoO_x-to-WO_x ratio of 1:1/3 were measured, and the results are shown in Figure 2c. The absorption edge of MoO_x is close to 460 nm, while it is around 465 nm for WO_x. After mixing the two oxides together, the absorption edge is relocated to 453 nm. Besides, a weak absorption is found for MoO_x in the long wavelength range, which implies that the defect density in the MoO_x is relatively low. On the other hand, the absorption curve of WO_x tails up significantly in the long wavelength range, indicating a high defect density. The absorption "tail" of the MoO_x/WO_x hybrid in the long wavelength range is located between that of the WO_x and MoO_x. In addition, the Raman spectra of the three materials were measured, and the results are shown in Figure 2d. Expectedly, typical fingerprint vibration modes at 288, 662, 818, and 994 cm^{-1} are observed on the MoO_x. More specifically, the Raman peak at 288 cm^{-1} represents the wagging mode of the double bond O═Mo═O, while Raman peaks at 662, 818, and 994.7 cm^{-1} represent the stretching mode of the triply coordinated oxygen (3Mo−O), doubly coordinated oxygen (2Mo−O), and terminal oxygen (Mo^{6+}−O), respectively.[47] As for the WO_x, Raman peaks at 717.7 and 807.2 cm^{-1} are observed, and they can be assigned to the O−W−O vibration and the stretching vibration of the bending oxygen of W−O−W, respectively.[48] Lastly, the Raman spectra

https://doi.org/10.1021/acsami.1c03848
ACS Appl. Mater. Interfaces 2021, 13, 33345−33353

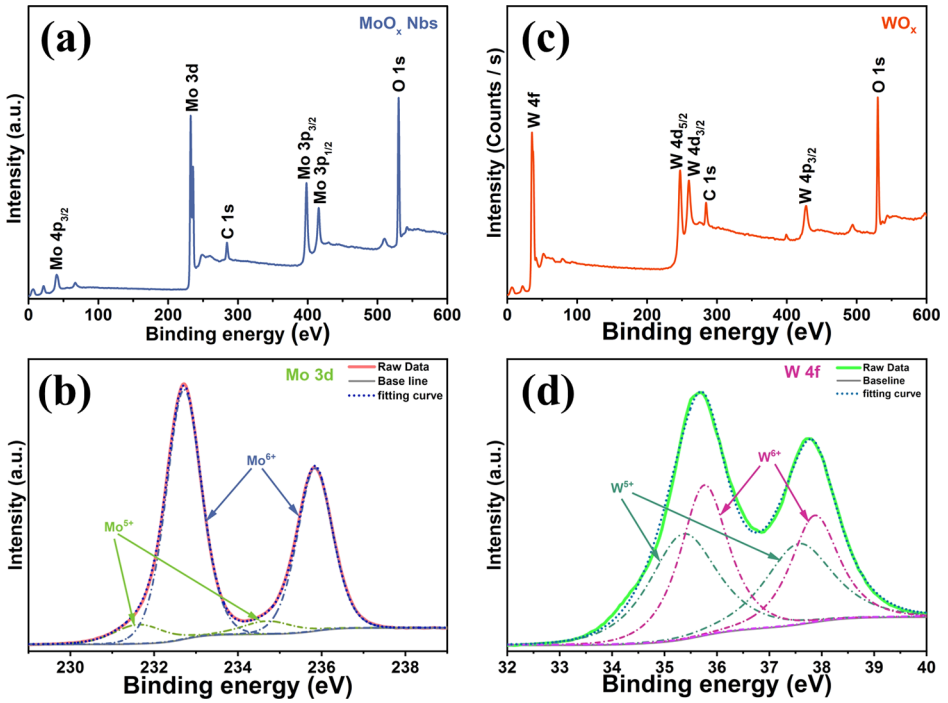

Figure 3. (a) Element survey spectrum of MoO_x Nbs. (b) Element survey spectrum of WO_x. (c) Deconvoluted core level spectra of Mo 3d measured on MoO_x Nbs. (d) Deconvoluted core level spectra of W 4f measured on WO_x.

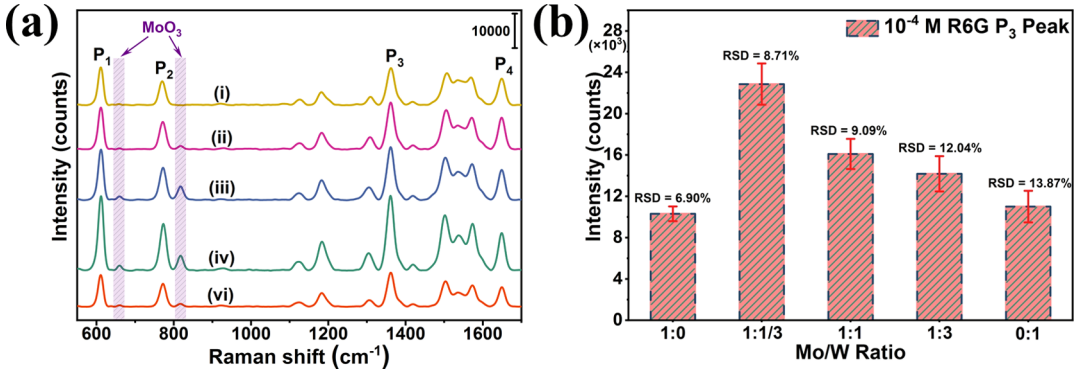

Figure 4. (a) Raman spectra measured on different substrates composed of Mo/W = 0:1 [curve: (i)], Mo/W=1:3 [curve: (ii)], Mo/W=1:1 [curve: (iii)], Mo/W = 1:1/3 [curve: (iv)], and Mo/W = 1:0 [curve: (vi)]. A R6G concentration of 10^{-4} M is used during the Raman measurement. (b) Comparison of the R6G P3 peak intensity obtained on different substrates.

of the MoO_x/WO_x hybrid are a superposition of the Raman peaks belonging to both MoO_x and WO_x.

To further explore the material property, X-ray photoelectron spectroscopy (XPS) was used to analyze the valence states of the element. Figure 3a,b shows the respective XPS survey spectra obtained on MoO_x and WO_x, with the Mo 3d, Mo 3p, W 4d, and O 1s peaks labeled. In the fine spectrum of MoO_x shown in Figure 3c, a twin-peak Mo 3d spectrum with Mo $3d_{3/2}$ at 235.84 eV and Mo $3d_{5/2}$ at 232.71 eV can be observed.[42] Through deconvolution analysis, it is found that MoO_x is mainly composed of Mo^{6+} ions (90.3%), with only a small percentage of Mo^{5+} (9.7%). These results are consistent with the low defect density as deduced from the absorption curve. A twin-peak W 4f spectrum with W $4f_{5/2}$ at 37.75 eV and W $4f_{7/2}$ at 35.69 eV is also seen in the fine spectrum of WO_x in Figure 3d. However, deconvolution analysis shows that WO_x is composed of 50.0% of W^{5+} ions and 50.0% of W^{6+} ions, indicating a high defect density[49] (consistent with the inference made from the absorption curve). Furthermore, XPS measurement was also performed on one of the MoO_x/WO_x hybrids. As shown in Figure S2a, three typical peaks assigned to Mo 3d, W 4d, and O 1s peaks can be observed on the survey spectrum. Detailed investigation on the binding energy of the Mo 3d peak in Figure S2b reveals a shift to a higher value by 0.3 eV, implying that electrons have been transferred from MoO_x to WO_x. This confirms the formation of a nano-heterojunction between the two oxides.[49]

The SERS characteristics of the MoO_x/WO_x hybrids were assessed using the R6G molecule as the Raman reporter. A total of 10 μL of 10^{-4} M R6G ethanol solution was dropped on the substrate, and then, the substrate was dried in the air. A 532 nm laser and 10 s integration time were used in the measurement. Figure 4 shows the SERS spectra collected on the substrates with different weight ratios. Four prominent Raman vibration modes of R6G are evidently enhanced on all five substrates. More specifically, the vibration modes at 609

https://doi.org/10.1021/acsami.1c03848
ACS Appl. Mater. Interfaces 2021, 13, 33345−33353

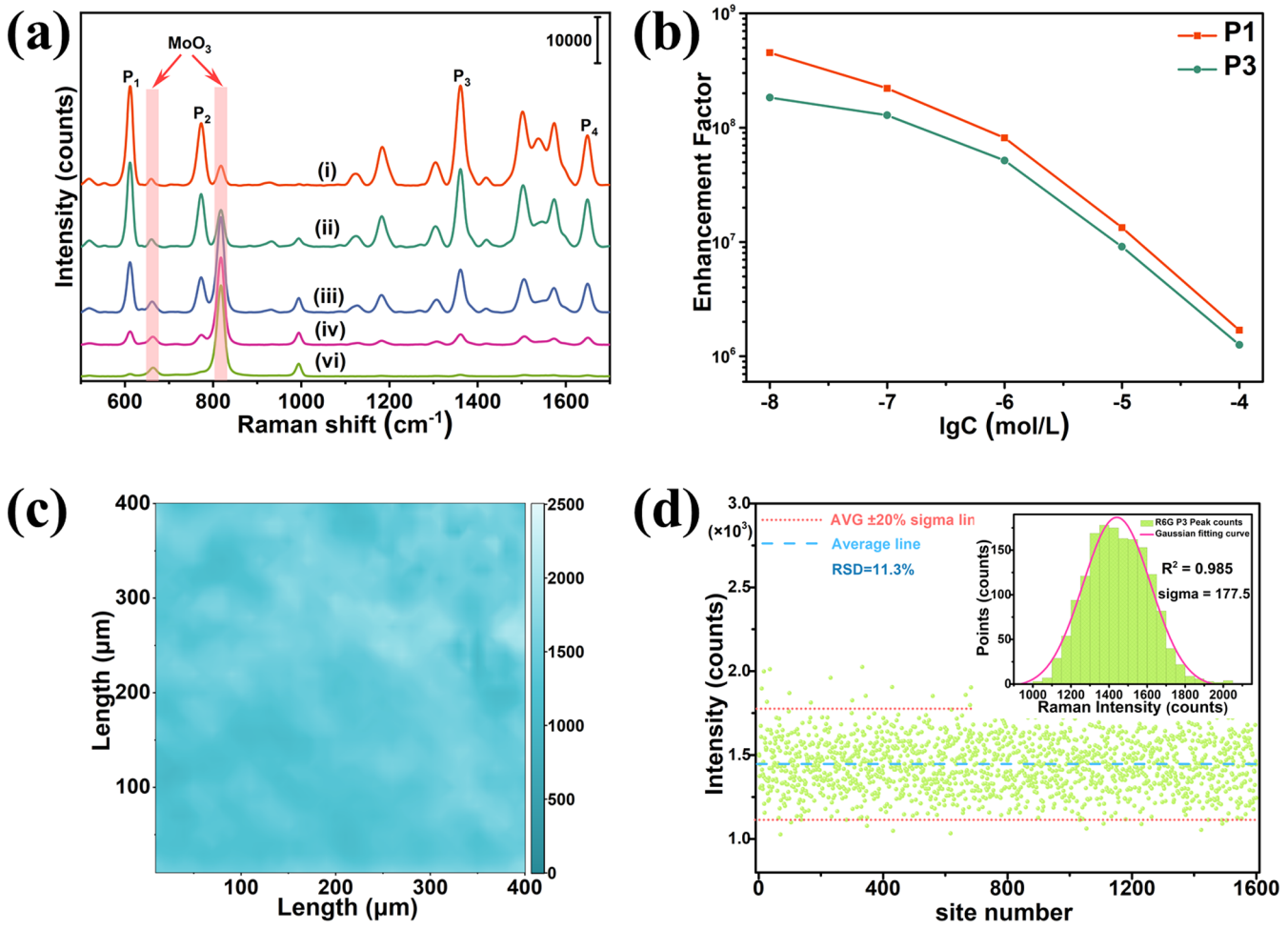

Figure 5. (a) Raman spectra measured on MoO_x/WO_x hybrids (1:1/3) when the concentration of R6G solution is 10^{-4} M [curve: (i)], 10^{-5} M [curve: (ii)], 10^{-6} M [curve: (iii)], 10^{-7} M [curve: (iv)], and 10^{-8} M [curve: (vi)]. (b) Calculated SERS EFs at different concentrations of R6G. (c) Raman mapping intensity at 1360 cm^{-1} obtained on a 400 × 400 μm^2 square with 10^{-7} M R6G as the reporter. (d) RSD of the mapped data points. The inset in panel (d) shows that the data points are fitted to Gaussian distribution.

(P1) and 772 cm^{-1} (P2) are attributed to the in-plane and out-of-plane bending modes of the aromatic C−H, respectively. The vibration modes at 1360 (P3) and 1637 cm^{-1} (P4) are assigned to the stretching vibrations of the aromatic C−C bonds.[50] At this moment, it is worth pointing out that the Raman vibration peaks from the oxide substrates are very weak and are found at wavelength numbers different from those of the R6G Raman vibration peaks. Hence, the former would not affect the R6G Raman signal intensity. Next, the enhancement capabilities of different substrates are evaluated using the peak intensity of P3 as the metric. It can be seen in Figure 4b that the P3 peak intensities obtained on three hybrids are twice as high as that obtained on the MoO_x or WO_x substrate. More interestingly, the largest improvement in the P3 peak intensity is obtained for the MoO_x/WO_x weight ratio of 1:1/3, whereas an increase in the ratio of WO_x in the hybrid results in the decrease in the peak intensity. This observation can be explained by the SEM images in Figure S1, which shows that in the situations of higher WO_x weight ratios, a piling up of the sea urchin-like WO_x structures occurs, resulting in a reduction in the number of heterojunctions and consequently the charge transfer efficiency. Other than the R6G, the SERS spectra of methylene blue (MB), rhodamine B (RhB), and crystal violet (CV) were also measured, and the results are shown in Figure S3. It can be observed that the hybrid oxide substrate also displays attractive Raman enhancement capability for molecules even far-off the resonance frequency.

In the next discussion, the substrate prepared using the MoO_x/WoO_x weight of 1:1/3 is chosen for estimating the SERS performance since this substrate gives the best SERS improvement. First, different R6G solution concentrations ranging from 10^{-4} to 10^{-8} M are used to evaluate the detection capability. As shown in Figure 5a, the Raman signals are still discernible even when the concentration reaches 10^{-8} M, indicating that the limit of detection can be as low as 10^{-8} M. Figure 5b shows that the enhancement factor (EF) obtained for the 10^{-7} M solution is in the order of 10^8 (see the Supporting Information for the calculation). The uniformity of the MoO_x/WO_x hybrid is also investigated. To achieve this, 10^{-7} M R6G ethanol solution was used as the reporter, and the integration time was reduced to 2 s for the purpose of expediting the experiment. The Raman signal intensity mapping was recorded on a randomly selected square with an area of 400 × 400 μm^2, and a total of 1600 points were measured. Figure 5c depicts the Raman signal intensity map for the 1360 cm^{-1} band, showing an average peak intensity of 1447 cps. The collected data points can be fitted to a Gaussian distribution (inset of Figure 5d), and the relative standard

https://doi.org/10.1021/acsami.1c03848
ACS Appl. Mater. Interfaces 2021, 13, 33345−33353

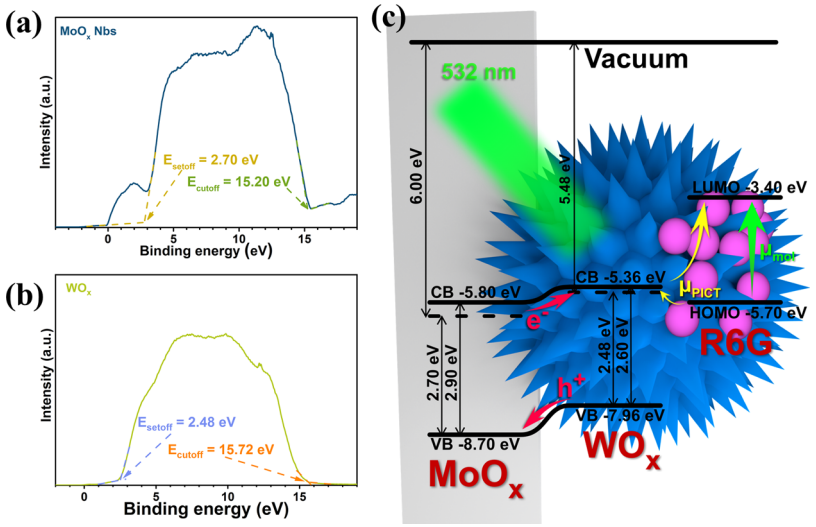

Figure 6. (a) UPS photoemission spectrum measured on MoO_x Nbs. (b) UPS photoemission spectrum measured on WO_x. (c) Band alignment between MoO_x and WO_x. The vacuum level is taken as the reference (0 eV).

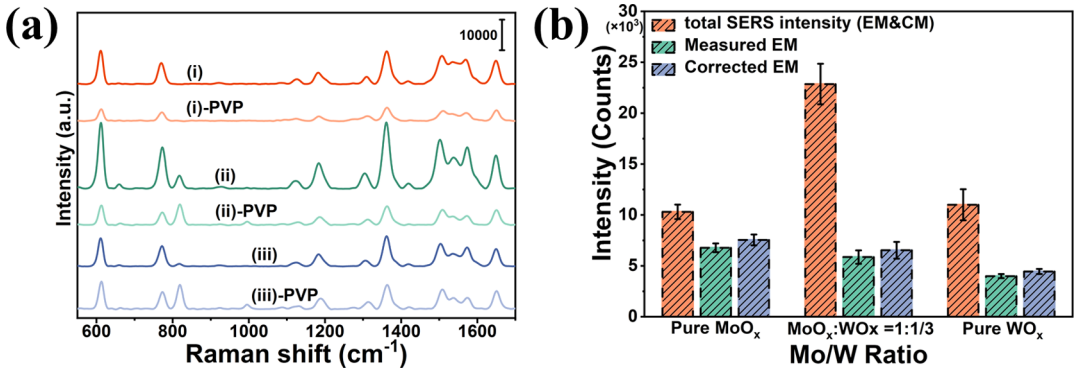

Figure 7. (a) SERS spectra measured on different hybrids with or w/o the PVP layer. Mo/W = 1:0 [curve: (i) and (i)-PVP], Mo/W = 1:1/3 [curve: (ii) and (ii)-PVP], and Mo/W = 0:1 [curve: (iii) and (iii)-PVP], hybrids with the PVP isolation layer are denoted with PVP. (b) Calculated contribution of EM and CM to the total SERS enhancement.

derivation is determined as 11.3%. The abovementioned results clearly show that the hybrid substrate with the optimal MoO_x/WO_x weight ratio possesses an excellent EF and uniformity, with good potential for ultralow trace detection.

Next, for the sake of understanding the SERS enhancement mechanism and unveiling the role of the nano-heterojunction in the charge transfer process, ultraviolet photoelectron spectroscopy (UPS) detection was performed to acquire the band alignment of the MoO_x/WO_x hybrid structure. Figure 6a shows the full photoemission spectrum of MoO_x. The extrapolated cutoff energy is found to be 15.2 eV, which indicates that the Fermi level of MoO_x is at −6 eV when the energy is referred to the vacuum level (0 eV). The extrapolated setoff energy is 2.7 eV, and thus, the top of the valence band (VB) of MoO_x is at −8.7 eV. Similarly, the full photoemission spectrum of WO_x in Figure 6b shows that the Fermi level is at −5.48 eV, and the top of the VB is at −7.96 eV (relative to the vacuum level at 0 eV). In addition, the band gaps of MoO_x and WO_x are extracted from their respective absorption spectra in Figure S4; they are 2.9 and 2.6 eV, respectively. Based on the abovementioned physical characterization data, the band alignment of two oxides is established and shown in Figure 6c. The conduction band (CB) and VB of WO_x are higher than the corresponding bands of MoO_x by 0.44 and 0.74 eV, respectively. Thus, a combination of these two oxides forms a staggered band structure with the internal electric field pointing from WO_x to MoO_x. To verify the formation of a heterojunction between the two oxides, a two-terminal device with a MoO_x/WO_x partial overlaid structure was fabricated (Figure S5a), and the photocurrent under the 532 nm laser illumination was measured. Figure S5b shows that a large photocurrent is obtained when the laser was shone on the MoO_x/WO_x hybrid structure. The large photocurrent may be ascribed to the incident photons generating many electron−hole pairs in the MoO_x/WO_x heterojunction. The built-in electric field separates the electron−hole pairs (with the electrons transferred to WO_x and the holes transferred to MoO_x), resulting in a photocurrent flowing in the external circuit. However, an extremely weak current is measured for the case where the MoO_x and WO_x structures were coated with PVP (polyvinyl pyrrolidone) (Figure S5b). Electron−hole pair generation is greatly suppressed in this case because the formation of a heterojunction was blocked by the PVP (Figure S5b). Furthermore, to analyze the electron transfer between the substrate and the molecules, the molecular orbitals of R6G are aligned to the band structure of the MoO_x/WO_x heterojunction (Figure 6c).[51] It can be seen that the CB of WO_x is 0.34 eV higher than the HOMO of the R6G. ζ

https://doi.org/10.1021/acsami.1c03848
ACS Appl. Mater. Interfaces 2021, 13, 33345−33353

potential measurement in Figure S6 reveals that WO_x is more negatively charged than MoO_x, implying that WO_x would tend to adsorb the more positively charged R6G molecules. Hence, during the SERS measurement, the electrons generated by the incident light are first separated and then accumulated on WO_x. These electrons are subsequently transferred from the CB of WO_x to the LUMO of R6G through the coupled molecular orbitals, resulting in the enhancement of the SERS signals.[52]

Lastly, to verify the mechanism understanding and to clarify the relative contributions of the EM and CM mechanisms to the total SERS enhancement in the hybrid oxide substrate, alternative SERS substrates were prepared using PVP as a barrier layer to cut off the charge transfer. Figure 7a shows the comparison of the SERS spectra recorded on the hybrid substrate with and without the PVP layer. With the incorporation of the PVP layer, part of the EM mechanism is attenuated, and the charge transfer path is blocked. The Raman signal intensity enhanced only by the EM mechanism is much lower than that measured on the normal substrates. The contributions of the EM and CM mechanisms are extracted from the two corresponding sets of Raman spectra (Table 1).

Table 1. SERS Intensity and EM and CM Contributions Obtained on Different Substrates

substrate types	total SERS intensity (counts)	EM measured (counts)	EM after correction (counts)	CM contribution (counts)
MoO_x	10,309	6773	7546	2763
WO_x	11,002	3991	4446	6556
MoO_x/WO_x hybrid (1:1/3)	22,856	5862	6532	16,323

As the PVP layer will attenuate the strength of the electric field that acts on the molecules, corrections are performed (see the correction of the EM in the Supporting Information). Figure 7b shows that both the EM and CM mechanisms contribute to the SERS enhancement on three substrates. More specifically, the corrected EM contribution obtained on the hybrid substrate (MoO_x/WO_x = 1:1/3) is about 1.47 times that of the WO_x substrate but is only 0.86 times that of the MoO_x substrate. On the other hand, the CM contribution obtained on the hybrid substrate is about 2.5 times and 5.9 times that of the WO_x and MoO_x substrates, respectively. The above-mentioned results present a clear distinction on the contributions of EM and CM to the total SERS enhancement. They also provide a solid support for our proposed role of nano-heterojunctions in enhancing the charge transfer efficiency in the hybrid oxide substrate.

3. CONCLUSIONS

In summary, we have developed a novel MoO_x/WO_x hybrid substrate for SERS measurement. Through aligning the band structure of MoO_x and WO_x, effective nano-heterojunctions are formed between the two oxide structures. The SERS performance is measured using a 532 nm laser as the excitation source and R6G molecule as the Raman reporter. About two times Raman signal intensity improvement can be achieved on the prepared MoO_x/WO_x hybrid substrate (of the corresponding weight ratio of 1:1/3) with an optimal number of nano-heterojunctions. The limit of detection can be as low as 10^{-8} M, and the EF can be as high as 10^8. Finally, mechanism analysis indicates that the attractive SERS performance may be attributed to the synergetic effect of the EM and CM mechanisms. More importantly, the formation of nano-heterojunctions can significantly promote the charge transfer efficiency, and the contribution of the CM mechanism on the MoO_x/WO_x hybrid substrate is about 2.5 times and 5.9 times that observed on the WO_x and MoO_x substrate, respectively.

4. MATERIALS AND EXPERIMENTAL METHODS

Chemicals. Ammonium molybdate tetrahydrate ($(NH_4)_6Mo_7O_{24}\cdot 4H_2O$, 99.0%), nitric acid ($HNO_3$, 65%), and absolute ethanol (C_2H_5OH, 99.7%) were purchased from Sinopharm Chemical Agent Co., Ltd. Rhodamine 6G (R6G) was bought from Sigma-Aldrich. L-(+)-Tartaric acid ($C_4H_6O_6$, 99.0%) was purchased from Shanghai Macklin Biochemical Co., Ltd. Tungsten chloride (WCl_6, 99.99%) was purchased from Aladdin Biochemical Technology Co., Ltd. Deionized water (18.2 MΩ·cm) was used for the preparation of samples. All chemicals used in this work were of analytic purity and used without further purification.

Synthesis of MoO_x. MoO_x was synthesized using a simple hydrothermal method. First, $(NH_4)_6Mo_7O_{24}\cdot 4H_2O$ (825 mg) and L-(+)-tartaric acid (400 mg) were dissolved in deionized water (50 mL), and then, the mixed solution was stirred for 30 min. Thereafter, nitric acid (1 mL) was added into the abovementioned mixed solution, stirring for another 10 min. After that, the mixed solution was transferred to a Teflon-lined stainless-steel autoclave and kept at 180 °C for 24 h. Finally, a milky white precipitate was collected by centrifugation (5000 rpm), washed with ethanol and DI water three times, and finally dried in a vacuum oven at 50 °C for 24 h for further use.

Synthesis of WO_x. WO_x was synthesized by a solvothermal method. WCl_6 (0.5 g) was used as a tungsten source and dissolved in ethanol (30 mL), stirring for 20 min. Thereafter, the mixed solution was transferred to a Teflon-lined stainless-steel autoclave and kept at 180 °C for 24 h. After that, blue color products were collected by centrifugation (10,000 rpm), washed with ethanol three times, and then dried in a vacuum oven at 60 °C for 24 h.

Coating PVP on the Surface of Nanoparticles. To isolate the charge transfer, PVP (20 mg) was first dissolved in DI water (100 μL), and then, the PVP solution (100 μL) was added into the nanoparticle solution (100 μL), stirring for 3 h to coat the PVP on the nanoparticle surface. Then, the nanoparticles were collected by centrifugation, washed with ethanol three times, and then dried in a vacuum oven at 60 °C for further use.

Preparation of the SERS Substrate. To construct the MoO_x/WO_x nano-heterojunction, different weight ratios of MoO_x and WO_x (MoO_x/WoO_x = 1:0, 1:1/3, 1:1, 1:3, and 0:1) were mixed in DI water (1 mL) and sonicated for 30 min. Then, the mixture (10 μL) was dropped onto a pre-cleaned silicon chip (5 × 5 mm^2) and dried in a vacuum oven at 50 °C for 5 h to obtain the SERS substrate.

Characterization. The XRD spectrum was recorded on a D8 Advance diffractometer equipped with a LynxEye XE detector (Bruker-AXS, Karlsruhe, Germany). SEM images were obtained using the Hitachi SU-70 system (Hitachi, Japan). XPS was performed using a Thermo Scientific K-Alpha instrument; the X-ray emission source is Al Kα rays ($h\nu$ = 1486.6 eV), and the test binding energy data were corrected to C 1s = 284.6 eV. UPS was performed using a Thermo ESCALAB XI+ instrument with the He I line as the ultraviolet emission source ($h\nu$ = 21.2 eV). Absorption−diffuse reflectance was measured with a fluorescence spectrophotometer (Cary Eclipse, USA). The ζ potential of WO_x, MoO_x, and the heterojunction in the solution was analyzed using a nanoparticle size potential analyzer (Malvern Zetasizer Nano ZS90). The photocurrent data were measured on the Keithley 2450 digital source meter (Tektronix, USA) with a 532 nm laser as the light source. SERS measurements were performed on the ProSp-Micro40-VIS Raman system (Hangzhou SPL) equipped with a QE Pro spectrometer (Ocean Optics, USA). A 532 nm semiconductor laser was used as the excitation source, and the diameter of the spot size was 20 μm (50×

https://doi.org/10.1021/acsami.1c03848
ACS Appl. Mater. Interfaces 2021, 13, 33345−33353

objective lens). The Raman spectra were collected under a laser power of 1 mW and an integration time of 10 s unless mentioned otherwise.

■ ASSOCIATED CONTENT

Supporting Information

The Supporting Information is available free of charge at https://pubs.acs.org/doi/10.1021/acsami.1c03848.

Additional characterization data, calculation of the enhancement factors, and correction of EM (PDF)

■ AUTHOR INFORMATION

Corresponding Authors

Chenjie Gu − *The Photonic Research Institute, Ningbo University, Ningbo 315211, China;* orcid.org/0000-0002-1339-4534; Email: guchenjie@nbu.edu.cn

Tao Jiang − *The Photonic Research Institute, Ningbo University, Ningbo 315211, China;* orcid.org/0000-0002-2429-3229; Email: jiangtao@enbu.edu.cn

Shuwen Zeng − *XLIM Research Institute, CNRS/University of Limoges, 87060 Limoges, France;* orcid.org/0000-0003-2188-7213; Email: shuwen.zeng@unilim.fr

Authors

Songyang Xie − *The Photonic Research Institute, Ningbo University, Ningbo 315211, China*

Dong Chen − *The Photonic Research Institute, Ningbo University, Ningbo 315211, China*

Ying Ying Wang − *Department of Optoelectronic Science, Harbin Institute of Technology at Weihai, Weihai 264209, China*

Zhenhua Ni − *School of Physics, Southeast University, Nanjing 211189, China;* orcid.org/0000-0002-6316-2256

Xiang Shen − *The Photonic Research Institute, Ningbo University, Ningbo 315211, China*

Jun Zhou − *The Photonic Research Institute, Ningbo University, Ningbo 315211, China*

Complete contact information is available at: https://pubs.acs.org/10.1021/acsami.1c03848

Author Contributions

⊥S.X. and D.C. contributed equally to this work.

Notes

The authors declare no competing financial interest.

■ ACKNOWLEDGMENTS

This research was funded by the National Natural Science Funding of China (grant nos. 61704095 and 61905161), the Natural Science Funding of Ningbo (grant no. 2019A610058), and the K. C. Wong Magna Fund in Ningbo University. This project has also received funding from the European Union's Horizon 2020 research and innovation program under the Marie Sklodowska-Curie grant agreement no. 798916.

■ REFERENCES

(1) Fleischmann, M.; Hendra, P. J.; McQuillan, A. J. Raman Spectra of Pyridine Adsorbed at a Silver Electrode. *Chem. Phys. Lett.* **1974**, *26*, 163−166.

(2) Albrecht, M. G.; Creighton, J. A. Anomalously Intense Raman Spectra of Pyridine at a Silver Electrode. *J. Am. Chem. Soc.* **1977**, *99*, 5215−5217.

(3) Jeanmaire, D. L.; Van Duyne, R. P. Surface Raman Spectroelectrochemistry: Part I. Heterocyclic, Aromatic, and Aliphatic Amines Adsorbed on the Anodized Silver Electrode. *J. Electroanal. Chem. Interfacial Electrochem.* **1977**, *84*, 1−20.

(4) Li, J.-F.; Zhang, Y.-J.; Ding, S.-Y.; Panneerselvam, R.; Tian, Z.-Q. Core-Shell Nanoparticle-Enhanced Raman Spectroscopy. *Chem. Rev.* **2017**, *117*, 5002−5069.

(5) Lee, H. K.; Lee, Y. H.; Koh, C. S. L.; Phan-Quang, G. C.; Han, X.; Lay, C. L.; Sim, H. Y. F.; Kao, Y.-C.; An, Q.; Ling, X. Y. Designing Surface-Enhanced Raman Scattering (SERS) Platforms beyond Hotspot Engineering: Emerging Opportunities in Analyte Manipulations and Hybrid Materials. *Chem. Rev.* **2019**, *48*, 731−756.

(6) Schatz, G. C.; Young, M. A.; Duyne, R. P. Electromagnetic Mechanism of SERS. In *Surface-Enhanced Raman Scattering-Physics and Applications*; Kneipp, K., Moskovits, M., Kneipp, J., Eds.; Springer: Berlin, 2006; Vol. *103*, pp 19−45.

(7) Ben-Jaber, S.; Peveler, W. J.; Quesada-Cabrera, R.; Cortés, E.; Sotelo-Vazquez, C.; Abdul-Karim, N.; Maier, S. A.; Parkin, I. P. Photo-Induced Enhanced Raman Spectroscopy for Universal Ultra-Trace Detection of Explosives, Pollutants and Biomolecules. *Nat. Commun.* **2016**, *7*, 12189.

(8) Du, Y.; Liu, H.; Chen, Y.; Tian, Y.; Zhang, X.; Gu, C.; Jiang, T.; Zhou, J. Recyclable Label-free SERS-based Immunoassay of PSA in Human Serum Mediated by Enhanced Photocatalysis Arising from Ag Nanoparticles and External Magnetic Field. *Appl. Surf. Sci.* **2020**, *528*, 146953.

(9) Laing, S.; Jamieson, L. E.; Faulds, K.; Graham, D. Surface-enhanced Raman Spectroscopy for In-vivo Biosensing. *Nat. Rev. Chem.* **2017**, *1*, 0060.

(10) Tian, Y.; Liu, H.; Chen, Y.; Gu, C.; Wei, G.; Jiang, T. Quantitative SERS-Based Detection and Elimination of Mixed Hazardous Additives in Food Mediated by the Intrinsic Raman Signal of TiO2 and Magnetic Enrichment. *ACS Sustainable Chem. Eng.* **2020**, *8*, 16990−16999.

(11) Ze, H.; Chen, X.; Wang, X.-T.; Wang, Y.-H.; Chen, Q.-Q.; Lin, J.-S.; Zhang, Y.-J.; Zhang, X.-G.; Tian, Z.-Q.; Li, J.-F. Molecular Insight of the Critical Role of Ni in Pt-Based Nanocatalysts for Improving the Oxygen Reduction Reaction Probed Using an In Situ SERS Borrowing Strategy. *J. Am. Chem. Soc.* **2021**, *143*, 1318−1322.

(12) Grzelczak, M.; Pérez-Juste, J.; Mulvaney, P.; Liz-Marzán, L. M. Shape Control in Gold Nanoparticle Synthesis. *Chem. Soc. Rev.* **2008**, *37*, 1783−1791.

(13) Zhang, J.; Li, X.; Sun, X.; Li, Y. Surface Enhanced Raman Scattering Effects of Silver Colloids with Different Shapes. *J. Phys. Chem. B* **2005**, *109*, 12544−12548.

(14) Lv, W.; Gu, C.; Zeng, S.; Han, J.; Jiang, T.; Zhou, J. One-Pot Synthesis of Multi-Branch Gold Nanoparticles and Investigation of Their SERS Performance. *Biosens. Bioelectron.* **2018**, *8*, 113.

(15) Jiang, T.; Chen, G.; Tian, X.; Tang, S.; Zhou, J.; Feng, Y.; Chen, H. Construction of Long Narrow Gaps in Ag Nanoplates. *J. Am. Chem. Soc.* **2018**, *140*, 15560−15563.

(16) Ma, Y.; Du, Y.; Chen, Y.; Gu, C.; Jiang, T.; Wei, G.; Zhou, J. Intrinsic Raman Signal of Polymer Matrix Induced Quantitative Multiphase SERS Analysis based on Stretched PDMS Film with Anchored Ag Nanoparticles/Au Nanowires. *Chem. Eng. J.* **2020**, *381*, 122710.

(17) Cardinal, M. F.; Vander Ende, E.; Hackler, R. A.; McAnally, M. O.; Stair, P. C.; Schatz, G. C.; Van Duyne, R. P. Expanding Applications of SERS through Versatile Nanomaterials Engineering. *Chem. Rev.* **2017**, *46*, 3886−3903.

(18) Niu, C.; Zou, B.; Wang, Y.; Cheng, L.; Zheng, H.; Zhou, S. Highly Sensitive and Reproducible SERS Performance from Uniform Film Assembled by Magnetic Noble Metal Composite Microspheres. *Langmuir* **2016**, *32*, 858−863.

(19) Ma, J.; Liu, X.; Wang, R.; Zhang, J.; Jiang, P.; Wang, Y.; Tu, G. Bimetallic Core−Shell Nanostars with Tunable Surface Plasmon Resonance for Surface-Enhanced Raman Scattering. *ACS Appl. Nano Mater.* **2020**, *3*, 10885−10894.

(20) Alessandri, I.; Lombardi, J. R. Enhanced Raman Scattering with Dielectrics. *Chem. Rev.* **2016**, *116*, 14921−14981.

(21) Yang, L.; Gong, M.; Jiang, X.; Yin, D.; Qin, X.; Zhao, B.; Ruan, W. Investigation on SERS of Different Phase Structure TiO_2 Nanoparticles. *J. Raman Spectrosc.* **2015**, *46*, 287−292.
(22) Otto, A. The "Chemical" (Electronic) Contribution to Surface-Enhanced Raman Scattering. *J. Raman Spectrosc.* **2005**, *36*, 497−509.
(23) Cong, S.; Yuan, Y.; Chen, Z.; Hou, J.; Yang, M.; Su, Y.; Zhang, Y.; Li, L.; Li, Q.; Geng, F.; Zhao, Z. Noble Metal-comparable SERS Enhancement from Semiconducting Metal Oxides by Making Oxygen Vacancies. *Nat. Commun.* **2015**, *6*, 7800.
(24) Jiang, X.; Song, K.; Li, X.; Yang, M.; Han, X.; Yang, L.; Zhao, B. Double Metal Co-Doping of TiO_2 Nanoparticles for Improvement of their SERS Activity and Ultrasensitive Detection of Enrofloxacin: Regulation Strategy of Energy Levels. *ChemistrySelect* **2017**, *2*, 3099−3105.
(25) Cheng, R.; Hu, T.; Hu, M.; Li, C.; Liang, Y.; Wang, Z.; Zhang, H.; Li, M.; Wang, H.; Lu, H.; Fu, Y.; Zhang, H.; Yang, Q.-H.; Wang, X. MXenes Induce Epitaxial Growth of Size-controlled Noble Nanometals: A Case Study for Surface Enhanced Raman Scattering (SERS). *J. Mater. Res. Technol.* **2020**, *40*, 119−127.
(26) Yin, Y.; Miao, P.; Zhang, Y.; Han, J.; Zhang, X.; Gong, Y.; Gu, L.; Xu, C.; Yao, T.; Xu, P.; Wang, Y.; Song, B.; Jin, S. Significantly Increased Raman Enhancement on MoX_2 (X = S, Se) Monolayers upon Phase Transition. *Adv. Funct. Mater.* **2017**, *27*, 1606694.
(27) Lin, J.; Hao, W.; Shang, Y.; Wang, X.; Qiu, D.; Ma, G.; Chen, C.; Li, S.; Guo, L. Direct Experimental Observation of Facet-Dependent SERS of Cu_2O Polyhedra. *Small* **2018**, *14*, 1703274.
(28) Ye, Y.; Yi, W.; Liu, W.; Zhou, Y.; Bai, H.; Li, J.; Xi, G. Remarkable Surface-enhanced Raman Scattering of Highly Crystalline Monolayer Ti_3C_2 Nanosheets. *Sci. China Mater.* **2020**, *63*, 794−805.
(29) Zhou, X.; Wu, D.; Jin, Z.; Song, X.; Wang, X.; Suib, S. L. Significantly increased Raman enhancement on defect-rich O-incorporated 1T-MoS_2 nanosheets. *J. Mater. Sci.* **2020**, *55*, 16374−16384.
(30) Zhang, Q.; Li, X.; Yi, W.; Li, W.; Bai, H.; Liu, J.; Xi, G. Plasmonic MoO_2 Nanospheres as a Highly Sensitive and Stable Non-Noble Metal Substrate for Multicomponent Surface-Enhanced Raman Analysis. *Anal. Chem.* **2017**, *89*, 11765−11771.
(31) Hou, X.; Lin, Q.; Wei, Y.; Hao, Q.; Ni, Z.; Qiu, T. Surface-Enhanced Raman Scattering Monitoring of Oxidation States in Defect-Engineered Two-Dimensional Transition Metal Dichalcogenides. *J. Phys. Chem. Lett.* **2020**, *11*, 7981−7987.
(32) He, R.; Lai, H.; Wang, S.; Chen, T.; Xie, F.; Chen, Q.; Liu, P.; Chen, J.; Xie, W. Few-layered vdW MoO_3 for Sensitive, Uniform and Stable SERS Applications. *Appl. Surf. Sci.* **2020**, *507*, 145116.
(33) Yue, X. F.; Liang, Y.; Jiang, J.; Liu, R. G.; Ren, S. T.; Gao, R. X.; Zhong, B.; Wen, G. W.; Wang, Y. Y.; Zou, M. Q. Raman Intensity Enhancement of Molecules Adsorbed onto HfS_2 Flakes up to 200 Layers. *Nanoscale* **2019**, *11*, 2179−2185.
(34) Luo, M.; Fan, T.; Zhou, Y.; Zhang, H.; Mei, L. 2D Black Phosphorus−Based Biomedical Applications. *Adv. Funct. Mater.* **2019**, *29*, 1808306.
(35) Li, Y.; Cheng, J.; Liu, Y.; Liu, P.; Cao, W.; He, T.; Chen, R.; Tang, Z. Manipulation of Surface Plasmon Resonance in Sub-Stoichiometry Molybdenum Oxide Nanodots through Charge Carrier Control Technique. *J. Mater. Chem. C* **2017**, *121*, 5208−5214.
(36) Zhang, Q.; Li, X.; Ma, Q.; Zhang, Q.; Bai, H.; Yi, W.; Liu, J.; Han, J.; Xi, G. A Metallic Molybdenum Dioxide with High Stability for Surface Enhanced Raman Spectroscopy. *Nat. Commun.* **2017**, *8*, 14903.
(37) Huang, Q.; Hu, S.; Zhuang, J.; Wang, X. MoO_{3-x}-Based Hybrids with Tunable Localized Surface Plasmon Resonances:Chemical Oxidation Driving Transformation from Ultrathin Nanosheets to Nanotubes. *Chem.—Eur. J.* **2012**, *18*, 15283−15287.
(38) Barbillon, G. Latest Novelties on Plasmonic and Non-Plasmonic Nanomaterials for SERS Sensing. *Nanomaterials* **2020**, *10*, 1200.
(39) Gu, C.; Li, D.; Zeng, S.; Jiang, T.; Shen, X.; Zhang, H. Synthesis and Defect Engineering of Molybdenum Oxides and Their SERS Applications. *Nanoscale* **2021**, *13*, 5620−5651.
(40) Wang, X.; Guo, L. SERS Activity of Semiconductors: Crystalline and Amorphous Nanomaterials. *Angew. Chem., Int. Ed.* **2020**, *59*, 4231−4239.
(41) Li, P.; Zhu, L.; Ma, C.; Zhang, L.; Guo, L.; Liu, Y.; Ma, H.; Zhao, B. Plasmonic Molybdenum Tungsten Oxide Hybrid with Surface-Enhanced Raman Scattering Comparable to that of Noble Metals. *ACS Appl. Mater. Interfaces* **2020**, *12*, 19153−19160.
(42) Niu, Z.; Zhou, C.; Wang, J.; Xu, Y.; Gu, C.; Jiang, T.; Zeng, S.; Zhang, Y.; Ang, D. S.; Zhou, J. UV-light-assisted Preparation of MoO_{3-x}/Ag NPs Film and Investigation on the SERS Performance. *J. Mater. Sci.* **2020**, *55*, 8868−8880.
(43) Xu, Y.; Lai, K.; Gu, C.; Jiang, T.; Shen, X.; Zeng, S.; Ho, A. H.-P.; Ang, D. S.; Zhou, J. Electrical Tuning of MoOx/Ag Hybrids and Investigation of their Surface-Enhanced Raman Scattering Performance. *Phys. Status Solidi RRL* **2020**, *15*, 2000499.
(44) Guo, Y.; Zhuang, Z.; Liu, Z.; Fan, W.; Zhong, H.; Zhang, W.; Ni, Y.; Guo, Z. Facile Hot Spots Assembly on Molybdenum Oxide Nanosheets via in situ Decoration with Gold Nanoparticles. *Appl. Surf. Sci.* **2019**, *480*, 1162−1170.
(45) Ghopry, S. A.; Alamri, M. A.; Goul, R.; Sakidja, R.; Wu, J. Z. Extraordinary Sensitivity of Surface-Enhanced Raman Spectroscopy of Molecules on MoS_2 (WS_2) Nanodomes/Graphene van der Waals Heterostructure Substrates. *Adv. Opt. Mater.* **2019**, *7*, 1801249.
(46) Li, M.; Fan, X.; Gao, Y.; Qiu, T. W18O49/Monolayer MoS2 Heterojunction-Enhanced Raman Scattering. *J. Phys. Chem. Lett.* **2019**, *10*, 4038−4044.
(47) Xie, F.; Choy, W. C. H.; Wang, C.; Li, X.; Zhang, S.; Hou, J. Low-Temperature Solution-Processed Hydrogen Molybdenum and Vanadium Bronzes for an Efficient Hole-Transport Layer in Organic Electronics. *Adv. Mater.* **2013**, *25*, 2051−2055.
(48) Zhou, C.; Sun, L.; Zhang, F.; Gu, C.; Zeng, S.; Jiang, T.; Shen, X.; Ang, D. S.; Zhou, J. Electrical Tuning of the SERS Enhancement by Precise Defect Density Control. *ACS Appl. Mater. Interfaces* **2019**, *11*, 34091−34099.
(49) Li, N.; Li, Y.; Li, W.; Ji, S.; Jin, P. One-Step Hydrothermal Synthesis of TiO_2@MoO_3 Core−Shell Nanomaterial: Microstructure, Growth Mechanism, and Improved Photochromic Property. *J. Phys. Chem. C* **2016**, *120*, 3341−3349.
(50) Dieringer, J. A.; Wustholz, K. L.; Masiello, D. J.; Camden, J. P.; Kleinman, S. L.; Schatz, G. C.; Van Duyne, R. P. Surface-Enhanced Raman Excitation Spectroscopy of a Single Rhodamine 6G Molecule. *J. Am. Chem. Soc.* **2009**, *131*, 849−854.
(51) Michaels, A. M.; Jiang; Brus, L. Ag Nanocrystal Junctions as the Site for Surface-Enhanced Raman Scattering of Single Rhodamine 6G Molecules. *J. Phys. Chem. B* **2000**, *104*, 11965−11971.
(52) Ganbold, E.-O.; Park, J.-H.; Dembereldorj, U.; Ock, K.-S.; Joo, S.-W. Charge-dependent Adsorption of Rhodamine 6G on Gold Nanoparticle Surfaces: Fluorescence and Raman Study. *J. Raman Spectrosc.* **2011**, *42*, 1614−1619.

https://doi.org/10.1021/acsami.1c03848
ACS Appl. Mater. Interfaces 2021, 13, 33345−33353